

REPORT DOCUMENTATION PAGE

Form Approved
OMB No. 0704-0188

Public reporting burden for this collection of information is estimated to average 1 hour per response, including the time for reviewing instructions, searching existing data sources, gathering and maintaining the data needed, and completing and reviewing this collection of information. Send comments regarding this burden estimate or any other aspect of this collection of information, including suggestions for reducing this burden to Department of Defense, Washington Headquarters Services, Directorate for Information Operations and Reports (0704-0188), 1215 Jefferson Davis Highway, Suite 1204, Arlington, VA 22202-4302. Respondents should be aware that notwithstanding any other provision of law, no person shall be subject to any penalty for failing to comply with a collection of information if it does not display a currently valid OMB control number. **PLEASE DO NOT RETURN YOUR FORM TO THE ABOVE ADDRESS.**

1. REPORT DATE (DD-MM-YYYY) 13-12-2011		2. REPORT TYPE Conference Paper		3. DATES COVERED (From - To)	
4. TITLE AND SUBTITLE Cryogenic High-Pressure Shear-Coaxial Jets Exposed to Transverse Acoustic Forcing				5a. CONTRACT NUMBER	
				5b. GRANT NUMBER	
				5c. PROGRAM ELEMENT NUMBER	
6. AUTHOR(S) Sophonias Teshome, Ivett Leyva, Douglas Talley, and Ann Karagozian				5d. PROJECT NUMBER	
				5f. WORK UNIT NUMBER 23080533	
7. PERFORMING ORGANIZATION NAME(S) AND ADDRESS(ES) Air Force Research Laboratory (AFMC) AFRL/RZSA 10 E. Saturn Blvd. Edwards AFB CA 93524-7680				8. PERFORMING ORGANIZATION REPORT NUMBER	
9. SPONSORING / MONITORING AGENCY NAME(S) AND ADDRESS(ES) Air Force Research Laboratory (AFMC) AFRL/RZS 5 Pollux Drive Edwards AFB CA 93524-7048				10. SPONSOR/MONITOR'S ACRONYM(S)	
				11. SPONSOR/MONITOR'S NUMBER(S) AFRL-RZ-ED-TP-2011-580	
12. DISTRIBUTION / AVAILABILITY STATEMENT Approved for public release; distribution unlimited (PA #111066).					
13. SUPPLEMENTARY NOTES For presentation at the 50 th AIAA Aerospace Sciences Meeting					
14. ABSTRACT This experimental study investigated the response of dynamic flow structures of cryogenic coaxial nitrogen jets to pressure perturbations due to transverse acoustic forcing at a pressure antinode (PAN). The role of injector exit geometry on the flow response was examined using two shear coaxial injectors with different outer-to-inner jet area ratios. Flow conditions for varying outer-to-inner jet momentum flux ratios (0.5 - 20), and acoustic pressure antinode at the jet axis location, under subcritical (reduced pressure of 0.44) chamber pressures were considered. Dark-core length measurements of the dense inner jet were used to indicate the extent of mixing under different flow conditions and exit geometries. A basic application of proper orthogonal decomposition on the intensity fluctuation of high-speed images enabled the extraction of the spatial and temporal characteristics of the dominant flow structures that existed in the flow field during exposure to acoustic forcing. Regardless of injector geometry or pressure regime, low outer-to-inner momentum flux ratio flows were found to be responsive to acoustic pressure antinode forcing. With increasing momentum flux ratio, however, the flow response to forcing depended on the injector geometry.					
15. SUBJECT TERMS					
16. SECURITY CLASSIFICATION OF:			17. LIMITATION OF ABSTRACT	18. NUMBER OF PAGES	19a. NAME OF RESPONSIBLE PERSON
a. REPORT	b. ABSTRACT	c. THIS PAGE			Dr. Douglas Talley
Unclassified	Unclassified	Unclassified	SAR	22	19b. TELEPHONE NUMBER (include area code) N/A

Cryogenic High-Pressure Shear-Coaxial Jets Exposed to Transverse Acoustic Forcing

Sophonias Teshome*

Department of Mechanical and Aerospace Engineering, UCLA, Los Angeles, CA 90095-1597

Ivett A. Leyva[†] and Douglas Talley[‡]

Air Force Research Laboratory, Edwards AFB, CA

Ann R. Karagozian[§]

Department of Mechanical and Aerospace Engineering, UCLA, Los Angeles, CA 90095-1597

This experimental study investigated the response of dynamic flow structures of cryogenic coaxial nitrogen jets to pressure perturbations due to transverse acoustic forcing at a pressure antinode (PAN). The role of injector exit geometry on the flow response was examined using two shear coaxial injectors with different outer-to-inner jet area ratios. Flow conditions for varying outer-to-inner jet momentum flux ratios (0.5 - 20), and acoustic pressure antinode at the jet axis location, under subcritical (reduced pressure of 0.44) chamber pressures were considered. Dark-core length measurements of the dense inner jet were used to indicate the extent of mixing under different flow conditions and exit geometries. A basic application of proper orthogonal decomposition on the intensity fluctuation of high-speed images enabled the extraction of the spatial and temporal characteristics of the dominant flow structures that existed in the flow field during exposure to acoustic forcing. Regardless of injector geometry or pressure regime, low outer-to-inner momentum flux ratio flows were found to be responsive to acoustic pressure antinode forcing. With increasing momentum flux ratio, however, the flow response to forcing depended on the injector geometry.

Nomenclature

A	area
a	vector of time-dependent amplitude coefficients
B	matrix of image pixel intensities
D	diameter
f	frequency
J	outer jet-to-inner jet momentum flux ratio, $\rho_o U_o^2 / \rho_i U_i^2$
m	no. of columns of pixels in a single image frame
\dot{m}	mass flow rate
N	no. of image frames
n	no. of rows of pixels in a single image frame
P	pressure
P_r	reduced pressure, P/P_{cr}
Q	matrix of column vectors, a
R	outer-to-inner jet velocity ratio, U_o/U_i
Re	Reynolds number

*Graduate Student Researcher, AIAA Student Member.

[†]Senior Aerospace Engineer, AIAA Member.

[‡]Principal Research Scientist, AIAA Member.

[§]Professor, AIAA Fellow.

S	outer-to-inner jet density ratio, ρ_o/ρ_i
T	temperature
U	jet velocity
V	matrix of column vectors, ϕ
ϕ	proper orthogonal mode
ρ	density

Subscript

i	pertaining to the inner jet
o	pertaining to the outer jet
F	acoustically forced

I. Introduction

Coaxial injectors have proven to be one of the most effective and simple means of delivering propellants in combustion devices such as in liquid rocket engines (LREs). Their application in LREs in the United States was seen as early as the development of the J-2 engine and as recently as the space shuttle main engine (SSME). Combustion instability is a phenomenon that can destroy an LRE in less than a second. It is primarily a result of feedback interactions between unsteady combustion rates and pressure fluctuations from acoustic modes in the combustion chamber. Since injector flows are directly involved in processes that take place inside combustors, it is crucial to understand how they contribute to, as well as how they are affected by, these unsteady physical mechanisms that lead to combustion instabilities. However, a successful understanding at a fundamental level of these interactions between injector flows and chamber phenomena can be aided by first isolating the fluid dynamics aspect from the reactive flow processes, and studying the coupling of non-reactive injector flow instabilities with external pressure perturbations.

Shear-coaxial jets consist of a circular core or inner jet and an annular or outer jet. In the near field region, where the potential cores of both the inner and outer jets exist, two shear-layers exist: an inner shear layer between the inner and outer jet flow, and an outer shear layer between the outer jet and the ambient fluid.¹ The development of instabilities in the individual shear layer, and the interaction between the two shear layers has a direct impact on the eventual instability characteristics of the entire flow field. Several studies²⁻⁴ investigate the existence and behavior of vortex structures in the near-field region of single-phase similar or different density coaxial jets. It is shown that for outer jet velocity (U_o) to inner jet velocity (U_i) ratios exceeding unity ($R = U_o/U_i > 1$), coherent structures in the outer shear layer dominate those in the inner shear layer.

The influence of these coherent structures on the overall dynamics of the flow field calls for an understanding of the factors leading to their formation. Detailed studies on the development and growth of natural instabilities in a single circular jet⁶ or a single circular jet with coflow⁷ reveal two of the most significant natural modes of instability: the axisymmetric and the first azimuthal or helical modes. These modes have comparable amplification rates over most of the core region downstream of the exit, with the helical mode eventually dominating the flow field farther downstream. It is shown¹ that the development of the outer shear layer of a coaxial jet behaves as the shear layer of a single jet, while the development of the inner shear layer behaves as that of a single jet issuing into an external coflow. Thus, the axisymmetric and helical modes of instability, along with natural as well as externally imposed flow conditions such as pressure or velocity perturbations, affecting their development, may be used to assess the stability of the coaxial jet.

Of equal importance in the application of coaxial jets is the mixing between the inner jet, usually the oxidizer, and the outer jet, the fuel. Since the growth and development of the shear layers is directly to the mixing of the two jets, one way of quantifying the degree of mixing is to determine the inner jet potential core length.^{1,8-10} The inner jet potential core ends once the inner shear layer converges on the jet axis. The current study does not involve detailed velocity profile measurements, but takes advantage of the dark images of back-lit dense inner jets, thus obtaining measurement of the dark-core length,^{13,14,17} which is related to the inner jet potential core length.

The present study continues the series of experimental studies done in the same facility,¹¹⁻¹⁷ which have examined the behavior of shear-coaxial N₂ jets at elevated pressures with and without the presence of a transverse acoustic field. It examines the baseline flow characteristics of two injectors with similar inner jet post thickness to diameter ratio, but different outer to inner jet area ratios, for different momentum

flux ratios. The present study also investigates the flow response to a pressure antinode forcing condition, where the coaxial jet is exposed to the maximum local pressure fluctuations in a transverse acoustic field. Dark-core length measurements are made to survey the effect of varying momentum flux ratios and that of the presence of acoustic forcing on the mixing behavior of the two jets. Unlike previous studies in the current facility, the present study applies a proper orthogonal decomposition (POD) analysis (see next section) to reduce the information obtained from a set of high-speed back-lit images in order to characterize the spatial and temporal behavior of dominant flow structures in the inner shear layer of the baseline and acoustically forced flows. Using this new approach, the goal is to gain a better understanding of the evolution of flow instabilities, and underline the critical differences in the flow stability characteristics brought about as a result of simple design alterations in the shear-coaxial injector.

II. Experimental Set-Up and Methods

These experiments were carried out at the Air Force Research Laboratory (AFRL), Edwards, test cell EC-4. Figure 1 shows a schematic of the experimental facility. The chamber was designed to operate at pressures spanning subcritical to supercritical pressures of N_2 , whose critical pressure is 3.4 MPa, and critical temperature is 126 K.

The inner and outer jets as well as the chamber pressurization flows were supplied by ambient temperature, high pressure nitrogen lines. Counter-flow heat exchangers using liquid nitrogen as the coolant fluid were used to cool the test fluids down to the desired temperatures. An unshielded Omega type-E thermocouple with a bead diameter of 0.25 mm was mounted on top of two linear positioning stages and placed near the injector to measure the radial temperature profile of the coaxial jet within one inner jet diameter from the exit plane. Porter mass flow meters (model 123-DKASVDAA) were used to measure the inner and outer jet flow rates, which were controlled via metering valves. The jets issued into the test section (Figure 1) of the inner chamber halfway between the two piezo-sirens located at opposite ends of the chamber. Each piezo-siren was fitted with a waveguide that transitioned from a circular cross-section to a rectangular one. The inner chamber was used to maximize the amplitude of acoustic oscillations generated by the piezo-sirens. However, both the inner and main chambers were maintained at the same static pressure, which was measured with a Stellar ST1500 pressure transducer. The outer to inner jet momentum flux ratio ($J = \rho_o U_o^2 / \rho_i U_i^2$), velocity ratio ($R = U_o / U_i$), and other flow conditions were determined based on thermophysical properties evaluated at the measured chamber pressure, and jet exit temperatures. Kulite absolute (CCQ-093) and differential (XCQ-093, XCE-093) pressure transducers were also used for making high-speed acoustic pressure measurements. These pressure transducers were placed along the inner chamber wall, where one transducer was located directly behind the jet, and two others inside the injector plenums.

The acoustic wave signals were generated using a Fluke 292 arbitrary waveform generator. A Trek PZD2000A high-voltage amplifier amplified continuous sine wave signals from the waveform generator before being input into each piezo-siren. The resulting acoustic waves from each piezo-siren were traveling waves that propagated transversely along the waveguide. Depending on the phase difference between the signals applied to each piezo-siren, a pressure antinode (PAN) condition, where the perturbation in pressure was maximum, or a pressure node (PN) condition, where the perturbation in pressure was minimum, could be created at the center of the chamber. Thus, using signals that were in-phase (0° phase difference), a PAN condition was established at the center of the waveguide, where the coaxial jets were situated.

Figure 2 shows a schematic of the injector exit with dimensional nomenclature, and Table II provides a summary of the injector exit dimensions under consideration. Both injectors were characterized by small lip thickness to inner diameter ratio t/D_1 , but one had a large outer-to-inner jet cross-sectional area ratio (LAR), while the other had a small area ratio (SAR).

Table 1. Injector exit dimensions (mm)

Injector	t	D_1	t/D_1	D_2	D_3	D_4	A_o/A_i
LAR	0.09	0.70	0.13	0.89	2.44	3.94	10.6
SAR	0.13	1.4	0.09	1.65	2.44	3.94	1.65

One of the main parameters used for assessing the effect of varying J values and the impact of the external

acoustic field on the coaxial jet mixing is the “dark-core” length of the inner jet measured from high-speed back-lit images. A xenon arc lamp was used to provide a back-lit image of the coaxial jet, which is visualized using a high speed Phantom v7.1 CMOS camera at framing rates exceeding 20 kHz. A detailed discussion of how the dark-core length is defined and measured has previously been reported¹³ and only a brief description will be given here. The original images (Figure 3a) are first converted, or thresholded, to a black and white image using the MATLAB subroutine “im2bw” (Figure 3b). The threshold level is determined using the MATLAB subroutine “graythresh”. This subroutine uses Otsu’s method¹⁸ and it is based on the zeroth and first cumulative moments of the gray-level histogram. Once a black and white image is obtained, the length of the jet is finally determined by drawing a contour around the black and white image and measuring the axial length of the longest contour attached to the injector as shown in Figure 3c.

Proper orthogonal decomposition (POD) of the high-speed images has proven to be a powerful means for extracting relevant qualitative and quantitative information from an otherwise complicated and noise-ridden set of image data. Thus, a pixel intensity data matrix, \mathbf{B} for a set of images may be represented^{19–21} as

$$\mathbf{B} = \sum_{k=1}^M a_k(t)\phi_k(x) \quad (1)$$

where a_k are vectors of temporal amplitude coefficients, ϕ_k are vectors of proper orthogonal modes, k is the mode number, and M is the number of modes. The decomposition was achieved by first arranging all the pixel intensity values of all frames into a single data array, whereby the pixel intensities from one frame occupied one row of the data array. Thus, a set of N consecutive frames, each of which had an n by m pixel resolution, constituted an N by $n \times m$ data array. The temporal mean of the data array was subtracted in order to eliminate the DC component of the intensity values resulting in a matrix $\tilde{\mathbf{B}}$ of intensity fluctuations. The method of singular value decomposition was implemented in MATLAB using a built-in subroutine to represent the matrix of intensity fluctuations as

$$\tilde{\mathbf{B}} = \mathbf{Q}\mathbf{V}^T \quad (2)$$

where \mathbf{Q} is an N by N matrix composed of column vectors a_k , and V is an N by $n \times m$ matrix composed of column vectors ϕ_k from Equation 1. The matrix \mathbf{Q} is the product of an orthogonal matrix of left singular vectors and a diagonal matrix of singular values of $\tilde{\mathbf{B}}$. The different modes were arranged in decreasing order of significance as dictated by the magnitude of the singular values of the decomposition.

In order to identify the existence of conjugate mode pairs,²⁰ which have a temporal phase difference of $\pm 90^\circ$ and also have similar ϕ_k , the cross-power spectral density of their amplitude coefficients, a_k and b_k was computed as

$$\text{CPSD} = \sum_{s=0}^{N-1} \text{corr}(a_k, b_k)e^{-i\omega s} \quad (3)$$

Here, $\text{corr}(a_k, b_k)$ represents the cross-correlation of a_k and b_k .

III. Results

All the experimental data presented here were obtained under subcritical (reduced pressure, $P_r = 0.44$) pressure conditions: the inner jet was in the liquid phase, while the outer jet was in the gas phase at temperatures well above the saturation temperature of N_2 . Tables of flow conditions and parameters are given in the Appendix. As previously noted, for coaxial jets of different densities, J is one of the governing parameters of coaxial jet mixing. However, for a set of test conditions in a particular pressure regime, the outer-to-inner jet density ratio ($S = \rho_o/\rho_i$) was held approximately constant while R was varied. Thus, the variation in J in these studies resulted mainly due the variation in R only.

III.A. Characterization of Dark-Core Lengths

The back-lit images were a result of non-uniform density in the coaxial jet flow field due to the difference in temperature of the inner and outer jets. Thus, the denser inner or core jet appears dark, hence the term “dark-core”. Hence, the length of dark-core downstream of the injector exit was used as an indicator of the extent of mixing between the inner and outer jets. In addition, although the end of the dark-core is not

coincident with the end of the potential core, it was nevertheless a good indicator of the extent of growth of the inner shear layer. The variation in the dark-core lengths with J will now be discussed for the two exit geometries.

Figures 4a and b show baseline flow (without acoustics) snapshot images for various J values using LAR and SAR injectors, respectively. The snapshots represent a single frame out of a set of images recorded at 25,000 fps for LAR and 20,000 fps for SAR under baseline conditions. The LAR injector flows showed a significant reduction in the axial dark-core lengths with increasing J . This was a direct outcome of the enhanced growth rate of the inner shear layer, which, in turn, resulted from the increased momentum flux defect between the inner and outer jets. In contrast, increasing J had a weaker influence on the dark-core length for the SAR injector. Due to the small hydraulic radius of the outer jet of the SAR injector, an effective entrainment of the inner jet fluid by the outer jet was limited to a relatively shorter distance from the exit plane resulting in longer dark-core lengths compared with the LAR injector for the same flow conditions.

Dark-core lengths were measured for a set of 1,000 image frames using the method described earlier. The measured mean dark-core lengths for each injector normalized by the respective D_1 are shown in Figure 5a with error bars denoting uncertainty in measurement from a single image. It should be noted that for such a large sample size, the uncertainties in the mean, given by the standard deviation of the mean ($\sigma_{mean} = \sigma/\sqrt{1000}$), of the measured dark-core lengths were negligible. It is clearly evident that the LAR injector flow underwent a significant change in the dark-core length with increasing J . For the lowest J values, since the dark-core exceeds the field of view of the image, the reported mean L_B/D_1 were inconclusive. The measured L_B/D_1 of the SAR injector¹⁷ flow confirmed the trend in the axial dark-core length already observed in the images.

The L_B/D_1 data in Figure 5a were replotted in Figure 5b corresponding to those for $J \geq 2$ in order to avoid dark-core images that exceed the image field of view. The data set for each injector was then fitted with a power curve-fit of the form CJ^{r^x} , where C and r are constants. It was found that $L_B/D_1 \propto J^{-0.39}$ for LAR injector flows and $L_B/D_1 \propto J^{-0.20}$ for SAR injector flows, thereby, yielding a quantitative variation of L_B/D_1 with J for each flow geometry. Included in Figure 5b is also a set of L_B/D_1 measurements¹⁷ for an exit geometry with large area ratio, similar to the LAR injector, but one with large t/D_1 ($t = 0.53$, $D_1 = 0.51$, $t/D_1 = 1.05$, $D_2 = 1.59$, $D_3 = 2.42$, $D_4 = 3.18$, $A_o/A_i = 12.9$). The results revealed that the dependence of L_B/D_1 on J was similar to that of the LAR injector. This may imply that the area ratio is a more important governing factor than t/D_1 when it comes to the variation with J of the extent of mixing of coaxial jets. However, more investigation must be done before generalizing this observation.

Figures 6a and 6b show acoustically forced flow (PAN condition) snapshot images for various J values at $P_r = 0.44$ using the LAR and SAR injectors, respectively. The LAR injector flows under a PAN condition exhibited a response that gradually seemed to be subdued at higher at larger J values. That is, the dark-core lengths at lower J values appeared to be noticeably shorter than their baseline counterparts, while at large J , they appeared indistinguishable from the corresponding baseline cases. On the other hand, the SAR injector flows under PAN condition resulted in flows that were significantly altered from the corresponding baseline cases regardless of J values.

These observations were further investigated using a plot of forced dark-core lengths, L , normalized by the corresponding baseline dark-core length, L_B , as shown in Figure 7. The forced LAR injector flow dark-core length was around 80% of that of the baseline at the lowest J , and showed a trend that gradually approached the baseline dark-core lengths with increasing J . On the contrary, SAR flows had dark-core lengths that were well below 80% that of baseline, hence, indicating a larger impact of the PAN condition.

III.B. Characterization of Dominant Flow Structures

Application of POD on the pixel intensity fluctuations in the high speed images, revealed spatial and temporal characteristics of the dominant periodic flow structures present in the coaxial jet flow. Figure 8a shows a snapshot image for $J = 0.5$ using the LAR injector. It shows a single frame out of a set of images recorded at 25,000 fps. A distinct difference between the snapshot and average images can be clearly seen by the absence of any discrete flow structures emanating from the dark-core at the jet interface boundary in the average image. These structures, which appear to be at least spatially periodic in Figure 8a, start forming by about $10D_1$. It is to be noted that the inner jet tube was not perfectly flush, but sticks out by about $0.2D_1$. This allowed for direct visual confirmation that the inner jet injector tube was not oscillating due to turbulent flow disturbances in the outer jet.

Figure 8c shows the first two proper orthogonal modes (POM) of the decomposition. As described in the

previous section, since only the fluctuation in intensity level was considered, the background fluid and the relatively uniform portion of the inner jet flow were subtracted out, thus depicted by a gray region to indicate a mean level in a gray-scaled image. On the other hand, the lighter and darker lobes represent, respectively, the presence and absence of flow structures emanating from the dense inner jet. Their spatial arrangement is indicative of the symmetry or antisymmetry of the flow structures formed in the inner shear layer. That is, at any given axial location, the presence of two similar lobes adjacent to each other indicates the presence of flow structures associated with axisymmetric instabilities in the shear layer. Meanwhile, opposite adjacent lobes indicate antisymmetry, which in axisymmetric flow geometries represents flow structures associated with helical instabilities. This is a viable assumption since under no external disturbances that can impose a preferential direction of oscillation to the shear-layer region, the only manner of propagation for the antisymmetric structures must be in the form of a helical disturbance. Hence, viewing the jet from two perpendicular lines of sight should reveal indistinguishable features for a baseline coaxial jet, as previously shown for some flow conditions.¹¹

The singular values of all modes of the decomposition are shown in Figure 9. POMs 1 and 2 in Figure 8c whose singular values correspond to modes 1 and 2, respectively, are seen to be the two most dominant flow structures. Moreover, the monotonically decreasing magnitude of the singular values with increasing mode numbers, and more than an order of magnitude difference between the highest and lowest modes implies that the more important flow dynamics were captured by the lower mode numbers. This is a direct outcome of a POD procedure, which orders the singular values, and their corresponding POMs, in order of decreasing importance.

The temporal characteristics of these dominant POMs were represented in the form of power spectral density of the temporal amplitude coefficients of the POD, and are shown in the plots in Figures 10a and 10b. The peaks located at the low end of the spectra were associated with the disturbance frequencies of the lobes identified in their respective POMs. Furthermore, a time-sequence of images of each individual POM revealed a progression of changes in the lobe pattern similar to that of a standing wave. That is, with every passing period associated with the characteristic peak frequencies, a light lobe turned dark, and vice-versa. On the other hand, a time-sequence of images of a superposition of the two POMs revealed a continuous propagation of the lobes traveling downstream of the injector exit.

This outcome is analogous to a simply demonstrable result that the superposition of two standing one-dimensional waves is a traveling wave, as long as the two standing waves are $\pm 90^\circ$ out-of-phase both temporally and spatially. In a similar manner, the cross-power spectral density (CPSD) of the temporal amplitude coefficients can be used to check the existence of a phase difference of $\pm 90^\circ$ at the frequencies near the peak of a CPSD magnitude spectrum. Figures 10c and 10d show the CPSD magnitude and phase plots of POMs 1 and 2. The phase plot shows that the temporal requirement to form a propagating disturbance was satisfied by structures whose frequencies were associated with a -90° phase difference. It can thus be concluded that the frequencies associated with the peak in the CPSD magnitude plot were the characteristic frequencies of the propagating disturbances seen in the time sequence of the superposed POMs. A similar analysis demonstrating the spatial requirement for forming a propagating disturbance has not been done in the current study. However, it should be sufficient to check that the two POMs have a similar lobe pattern. Hereafter, images of POMs presented will be the superposition of conjugate modes.

The location downstream of the injector exit, where the helical disturbances begin to dominate the inner shear layer region also decreased with increasing J . This is in accordance with the well known progression of development of shear-layer instabilities in axisymmetric single or coaxial jets.^{6,7} In the region close to the jet exit, where the shear-layer momentum thickness is very small compared to the jet diameter ($D/\theta \gg 1$), all modes of instability have been shown to have the same growth rates, with the axisymmetric and helical instability growth rates remain significant and comparable while that of the others become negligible. At the end of the potential core, however, the growth rate of helical instabilities becomes the most prevalent. Therefore, what the POMs show may well be the helical mode of instability of the jet.

Figures 11a-11d and Figures 12a-d show the snapshot, average, and POM images for LAR and SAR injector flows, respectively, for increasing J values. Figures 11e-h and Figures 12e-h show the corresponding CPSD magnitude spectra. Clearly, the LAR injector flows had dominant structures with peak frequencies that became broader and moved to higher frequencies as J increased. This behavior was in line with analytical results⁷ that with increasing coflow velocity, the region of unstable frequencies becomes broader and that the peak of the spatial growth rates shift to higher frequencies. On the contrary, as the CPSD magnitude spectra for the SAR injector flows show, the peak frequencies were unaffected by increasing J .

This contradiction to the expected behavior⁷ may again be explained by how soon the inner and outer jets attain a single jet behavior, thereby rendering the effect of coflow nonexistent.

Another notable outcome from the spectra in Figures 11e-h was that the peak frequencies were not dependent on R or J , but on the magnitude of the outer jet velocity. Despite the significant rise in R or J from Figure 11g-h, the peak for the latter sat at a slightly lower frequency. In order to investigate this, downstream convection velocities, U_s , of the dominant periodic structures depicted in the POM images were estimated based on the relation $U_s = \lambda f_s$, where λ is the wavelength measured from the images, and f_s is the characteristic frequency. The frequency, f_s , was obtained from the frequency that corresponded to the maximum CPSD magnitude that was closest to a CPSD phase of $\pm 90^\circ$ as illustrated in Figure 10c and 10d. The estimated U_s along with exit velocity of the inner jet, outer jet, and their mean are shown in Figure 13a for the LAR injector and Figure 13b for the SAR injector. For uniform density coaxial jets, the inner shear layer convection velocity may be approximated by the mean velocity. On the other hand, for variable density jets, as it is the case in this study, the shear-layer velocity is less than the mean velocity when the high-velocity jet is less dense.²² The estimated values of U_s for both the LAR and SAR injector flows depict this. However, U_s for LAR flow appear to closely depend on the magnitude of U_2 more than do those for SAR flow. This may be an indication that in the LAR geometry, the outer jet velocity governed the dynamics of the inner shear layer structures. However, further investigation will need to be done to generalize this outcome.

The PAN condition established a region of locally maximum pressure fluctuation in the vicinity of the coaxial jets so that the velocity fluctuation was minimum or non-existent in the ideal case. As pressure is a scalar physical quantity, PAN can essentially be regarded as a condition that creates a symmetric fluctuation in pressure about the jet center plane that is normal to the transverse direction of propagation of the acoustic waves.

Figure 14 shows the flow response under PAN condition for the same case in Figure 8 without acoustics. The snapshot image in Figure 14a clearly depicts a series of orderly structures formed along almost the entire inner jet column. They appear to have started forming near the injector exit, and grew as they propagated farther downstream due to the entrainment effect of the outer jet. This planar view of the structures depicts them as varicose instability structures in a planar jet. As a matter of fact, varicose instability plays a similar role in planar jets as does axisymmetric instability in round jets.²⁶ The POMs shown in Figure 10(c) give further evidence of the symmetric structures that started forming immediately downstream of the injector exit, and spread as they traveled downstream.

Another unique nature of the flow response to PAN forcing is depicted in Figures 15, 16a and 16b. Figure 15 shows that the flow response to PAN forcing represented by POMs 1 and 2 in Figure 8c was the dominant type of response. The relative magnitudes of all other modes were similar to those for the baseline shown in Figure 9. Moreover, the spectral plots in Figures 16a and 16b associated with POMs 1 and 2 indicate that the orderly structures had a characteristic frequency that was identical to the forcing acoustic frequency, f_F . This may seem to be a trivial outcome of external forcing, yet it does tell a lot about the nature of the flow stability as will be discussed below. Figure 16c shows the CPSD magnitude of the forced conjugate modes overlaid with the one for the baseline conjugate modes in Figure 10c. It shows that f_F completely overtook the baseline characteristic frequencies, which are no longer visible in the spectra of the PAN condition.

Figures 17 and 18 present the forced counterparts to the baseline cases presented in Figures 11 and 12 for the LAR and SAR injector flows, respectively. The lobe patterns visible in the POMs of the LAR flows showed a peculiar transition with increasing J . The lower J values (Figures 14c and 17a) showed a symmetric lobe pattern due to PAN forcing, whereas with increasing J , the symmetry became more skewed, and eventually turned into an antisymmetric pattern identical to the baseline cases. As noted earlier, antisymmetric pattern is the two-dimensional representation of a helical disturbance. Thus, for the LAR geometry, it can be concluded that the dominant flow response to PAN forcing at low J is in the form of amplified symmetric disturbances, while that at higher J transitions to helical disturbances identical to those present in flows without acoustic forcing.

The temporal characteristics of the flow response to the acoustic forcing are shown in the spectral plots in Figures 17e-h and 18e-h overlaid with the baseline spectra. The spectral content of the lower J values (Figures 16c and 17e) was such that during forcing, a peak in the magnitude at f_F completely took over the low peak frequencies of the baseline flows. As J increased, the significance of the peak at f_F relative to the baseline peak frequencies became more and more diminished, and the forced spectra began retaining more of the baseline spectra, as clearly evident in the highest J attained in Figure 17h. In other words, the

spectral energy contained at f_F for lower J values was less so at higher J values.

The response of the SAR injector flows to PAN forcing were drastically different from that of the LAR injector as shown in Figures 18. For lower J values ($J = 2.0, 5.2$), strong symmetric disturbances annihilate the inner jet flow. For higher J values ($J = 12, 17$), although symmetric disturbances were not as strong as in the lower J cases, they nevertheless were still prevalent as evident in the POM images and the spectra. As a matter of fact, the spectra showed strong response to external forcing regardless of the J value. This was again evident by the lack of any remnants of the low-frequency peaks present in the baseline spectra.

From a practical standpoint, it is crucial to ensure that the injector flow under non-design operating conditions behave as closely as possible to that under design operating conditions. Flow disturbances that arise as a result of acoustic instabilities due to excitation of the combustion chamber acoustic modes are typical instances of non-design operating conditions. Although special cases of the chamber acoustic behavior can be modeled and incorporated in the design considerations, a great many other unpredictable scenarios exist. Hence, the best approach is to implement a robust design that renders more predictable flow behavior for a given set of flow conditions regardless of any externally imposed disturbances. In light of this argument, LAR would be considered a preferable design configuration solely on the fact that it has been shown to be less sensitive to external disturbances at high J values.

IV. Conclusions

This experimental study examined the mixing behavior as well as the dominant periodic flow structures that develop in the inner shear layer of nonreactive shear-coaxial jets with and without the presence of transverse acoustic forcing. Flow conditions in subcritical pressure regimes and spanning a range of outer to inner jet momentum flux ratios, J , were investigated using two injector geometries. It was found that increasing J reduced the dark-core lengths of the large outer-to-inner jet area ratio (LAR) injector baseline flows more than the small outer-to-inner jet area ratio (SAR) injector baseline flows. This was indicative of more enhanced mixing of the inner and outer jets with increasing J for the LAR injector flows than for the SAR injector flows. Moreover, it was found that the dark-core lengths of the SAR injector flows were significantly shorter under PAN forcing for a given J than those of the LAR injector flows.

A proper orthogonal decomposition of pixel intensity fluctuation data revealed both the spatial and temporal characteristics of the inner shear layer flow structures. The LAR injector baseline flows exhibited helical instabilities at far enough downstream locations regardless of J . The frequencies of the flow structures associated with these helical instabilities shifted to higher frequencies with increasing magnitudes of jet velocities. Pressure antinode (PAN) acoustic forcing of low J LAR injector flows showed strong response by forming symmetric structures whose frequencies were identical with the forcing frequencies. Magnitude spectral plots also showed large peaks at the forcing frequencies and the baseline flow peak frequencies were completely removed from the forced spectra. With increasing J , however, the response to forcing became gradually weaker, and the broad baseline peak frequencies coexisted with the peaks at the forcing frequency.

The SAR injector baseline flows also exhibited helical instabilities. However, unlike LAR, the frequencies of the flow structures did not show significant shift to higher frequencies with increasing jet velocities. In addition, regardless of J , they showed strong response to PAN forcing. Thus, due to their readily responsiveness to external acoustic forcing, SAR injector flows may be regarded as a class of flows that display convectively unstable behavior. On the contrary, LAR injector flows appeared to display a transition from convectively unstable to absolutely unstable flow behavior with increasing J . This makes LAR injector flows at large enough J more desirable from a design standpoint since they behave in a predictable manner despite externally imposed disturbances such as those that arise due to the excitation of combustion chamber acoustic modes.

For a given geometry, the nature of the flow response to an external disturbance depending on the flow condition, namely J , may be used to characterize the state of stability of the flow. Previous works²³⁻²⁵ on flow stability characterize convectively unstable flows as noise amplifiers; that is, they are prone to external flow disturbances such as acoustic disturbances used in this study. Their spectral characteristics are such that when exposed to external forcing, their natural instabilities are completely removed and replaced by instabilities whose frequency match those of the forcing frequency.²⁷ Absolutely unstable flows, on the other hand, are characterized as naturally self-excited flows that do not respond well to external disturbances. Their spectra preserve the natural instabilities with or without a coexisting frequency content associated with the forcing frequency. These and the flow responses observed may be used to argue that the LAR flows

can be characterized as convectively unstable for low J flows, and transition into absolutely unstable flows with increasing J values, while the SAR flows depicted the behavior of convectively unstable flows. However, this characterization deserves further exploration in future studies.

Acknowledgments

The authors would like to thank Mr. Randy Harvey for his invaluable contributions in running and maintaining the experimental facility. They express their appreciation to Dr. Juan Rodriguez for providing the image data for the SAR injector. They also would like to thank Mr. Brian Newkirk, Mr. David Hill, Mr. Earl Thomas and Mr. John Hasier for providing technical assistance while running the experiments. This work is sponsored by AFOSR under Dr. Mitat Birkan, program manager.

References

- ¹Ko, N. W. M. and Kwan, S. H. 1976 The initial region of subsonic coaxial jet. *J. Fluid Mech.* 73, 305-332.
- ²Dahm, W. J. A., Frieler, C.E., and Tryggvason, G. 1992 Vortex structure and dynamics in the near field of a coaxial jet. *J. Fluid Mech.* 241, 371-402.
- ³Wicker, R.B. and Eaton, J.K. 1994 Near Field of a Coaxial Jet With and Without Axial Excitation. *AIAA Journal* 32, 542-546.
- ⁴Balarac, G., Mtais, O. and Lesieur, M. 2007 Mixing enhancement in coaxial jets through inflow forcing: A numerical study. *Phys. Fluids* 19, 075102.
- ⁵Gladnick, P. G., Enotiadis, A. C., LaRue, J. C. and Samuelsen, G. S. 1990 Near-field characteristics of a turbulent coflowing jet. *AIAA Journal* 28, 1405-1414.
- ⁶Cohen, J. and Wagnanski, L. 1987 The Evolution of Instabilities in an Axisymmetric Jet, Part I. Linear Growth of Disturbances Near the Nozzle. *J. Fluid Mech.* 176, 191-219.
- ⁷Michalke, A. and Hermann, G. 1982 On the inviscid instability of a circular jet with external flow. *J. Fluid Mech.* 114, 343-359.
- ⁸Mayer, W. and Krülle, G. 1995 Rocket Engine Coaxial Injector Liquid-Gas Interface Flow Phenomena. *J. Propulsion and Power* 11, 3.
- ⁹Villermaux, E., Rehab, H. and Hopfinger, E.J. 1994 Breakup Regimes and Self-Sustained Pulsations in Coaxial Jets. *Meccanica* 29, 393-401.
- ¹⁰Rehab, H., Villermaux, E. and Hopfinger, E.J. 1997 Flow regimes of large-velocity-ratio coaxial jets. *J. Fluid Mech.* 345, 357-381.
- ¹¹Davis, D.W., "On the behavior of a shear-coaxial jet, spanning sub- to supercritical pressures, with and without an externally imposed transverse acoustic field. Ph.D. Thesis," Penn State University, 2005.
- ¹²Davis, D.W. and Chehroudi, B. 2007 Measurements in an Acoustically Driven Coaxial Jet under Sub-, Near-, and Supercritical Conditions. *J. Propulsion and Power* 23, 2.
- ¹³Leyva, I. A., Chehroudi, B., Talley, D., "Dark-core analysis of coaxial injectors at sub-, near-, and supercritical conditions in a transverse acoustic field", *54th JANNAF Meeting*, Denver, CO, May 14-18, 2007.
- ¹⁴Leyva, I.A., Chehroudi, B. and Talley, D., "Dark-core analysis of coaxial injectors at sub-, near-, and supercritical pressures in a transverse acoustic field". *43rd AIAA/ASME/SAE/ASEE Joint Propulsion Conference and Exhibit*, AIAA 2007-5456.
- ¹⁵Leyva, I.A., Rodriguez, J.I., Chehroudi, B. and Talley, D. Preliminary, "Results on Coaxial Jet Spread Angles and the Effects of Variable Phase Transverse Acoustic Fields. *46th AIAA Aerospace Sciences Meeting and Exhibit*, AIAA 2008-950.
- ¹⁶Rodriguez, J. I., Graham, J. J., Leyva, I. A., Lyu, H.-Y., Talley, D., "On the Inner Jet Spread Angles of Coaxial Jets from Subcritical to Supercritical Conditions with Preliminary Numerical Results", *55th JANNAF Propulsion/4th Liquid Propulsion Subcommittee Meeting*, Orlando, FL, December 8-12, 2008.
- ¹⁷Rodriguez, J. I., "Acoustic Excitation of Liquid Fuel Droplets and Coaxial Jets," Ph.D. Thesis, University of California, Los Angeles, 2009.
- ¹⁸Otsu, N. 1979 A threshold selection method from gray-level histograms. *IEEE transactions on Systems, Man, and Cybernetics* 9, 62-66.
- ¹⁹Chatterjee, A. 2000 An introduction to the proper orthogonal decomposition. *Current Science* 78, 7.
- ²⁰Arienti, M, and Soteriou, M.C. 2009 Time-resolved proper orthogonal decomposition of liquid jet dynamics. *Phys. Fluids* 21, 112104.
- ²¹Narayanan, V., Lightfoot, M.D.A, Schumaker, S.A., Danczyk, S.A., and Eilers, B., "Use of Proper Orthogonal Decomposition Towards Time-resolved Image Analysis of Sprays," ILASS Americas, *23rd Annual Conference on Liquid Atomization and Spray Systems*, Ventura, CA, May 2011
- ²²Dimotakis, P.E. 1986 Two-Dimensional Shear-Layer Entrainment. *AIAA Journal* 24, 11.
- ²³Huerre, P. and Monkewitz, P.A. 1990 Local and Global Instabilities in Spatially Developing Flows. *Annu. Rev. Fluid Mech.* 22, 473-537
- ²⁴Huerre P. 2000. Open shear flow instabilities. In *Perspectives in Fluid Dynamics*, ed. G.K. Batchelor, H.K. Moffatt, M.G. Worster, pp. 159-229. Cambridge, UK: Cambridge Univ.
- ²⁵Jendoubi, S. and Strykowski, P.J. 1994 Absolute and convective instability of axisymmetric jets with external flow. *Phys. Fluids* 6, 3000.

²⁶Sevilla, A., Gordillo, J. M. and Martnez-Bazn, . 2002 The effect of the diameter ratio on the absolute and convective instability of free coflowing jets. *Phys. Fluids* 14, 3028.

²⁷Megerian, S., Davitian, J., Alves, L. S. de B. and Karagozian, A. R. 2007 Transverse jet shear-layer instabilities. Part 1. Experimental studies. *J. Fluid Mech.* 593, 93-129.

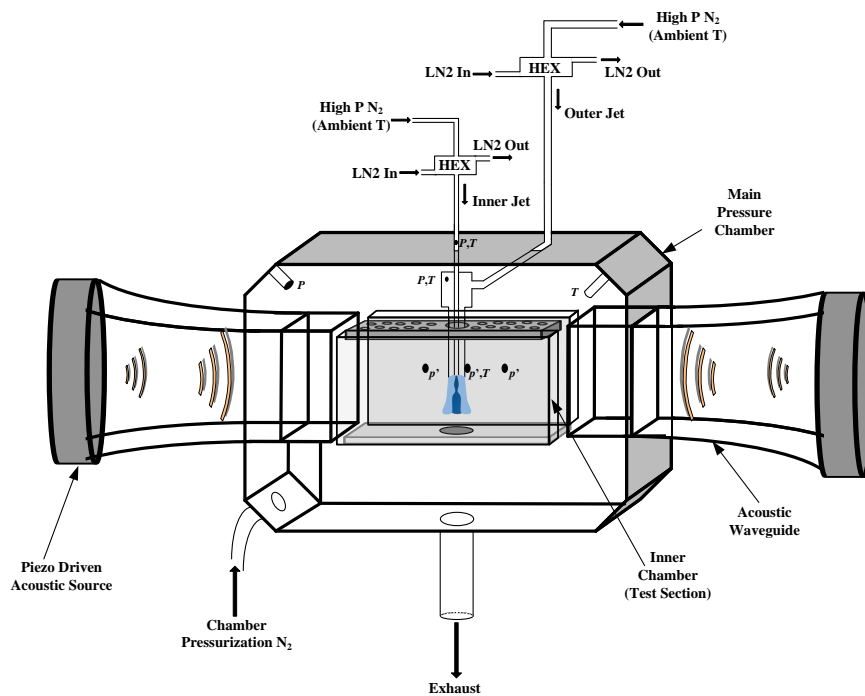


Figure 1. A schematic of the chamber and peripheral lines.

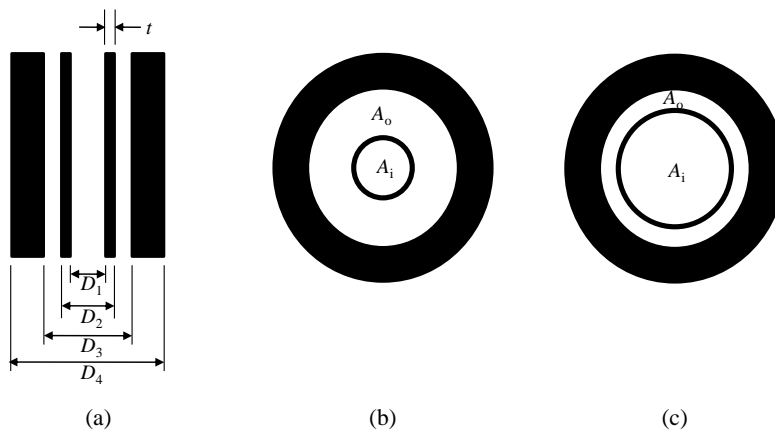


Figure 2. Injector geometry schematic: (a) axial cross-sectional view, (b) LAR exit configuration, (c) SAR exit configuration.

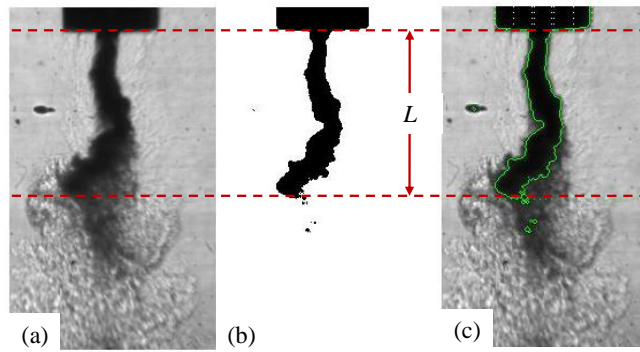


Figure 3. Measurement of dark-core length: (a) original image (b) black and white image after thresholding (c) Contour used to define the dark-core length (L).

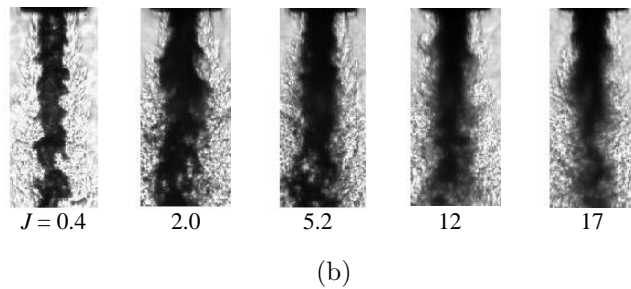
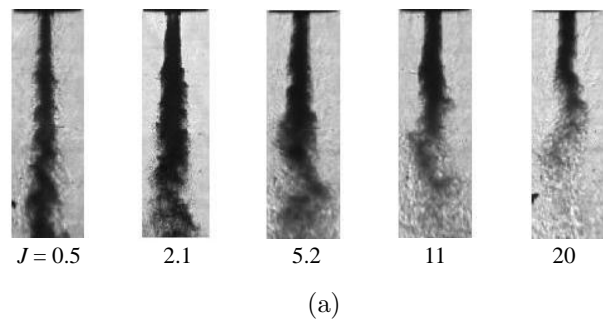
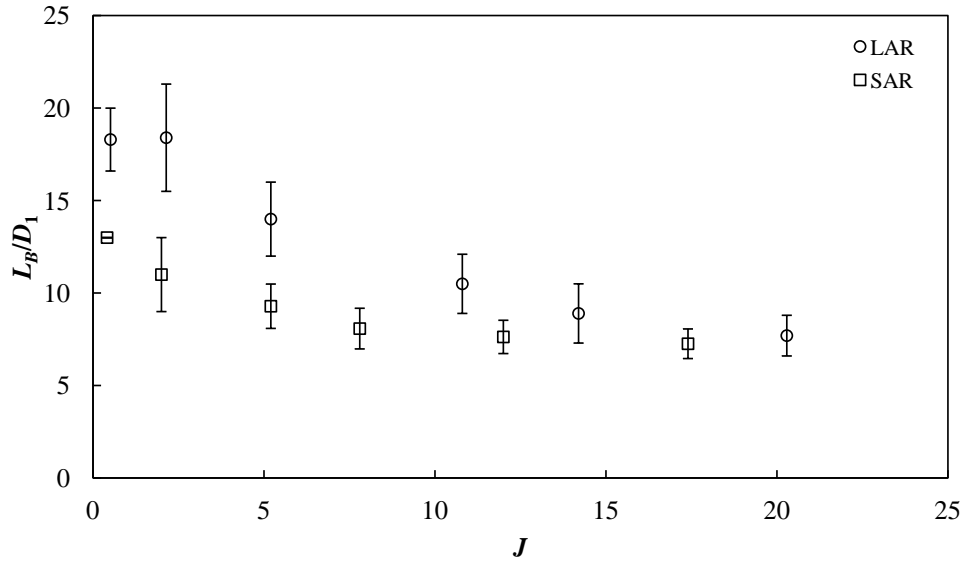
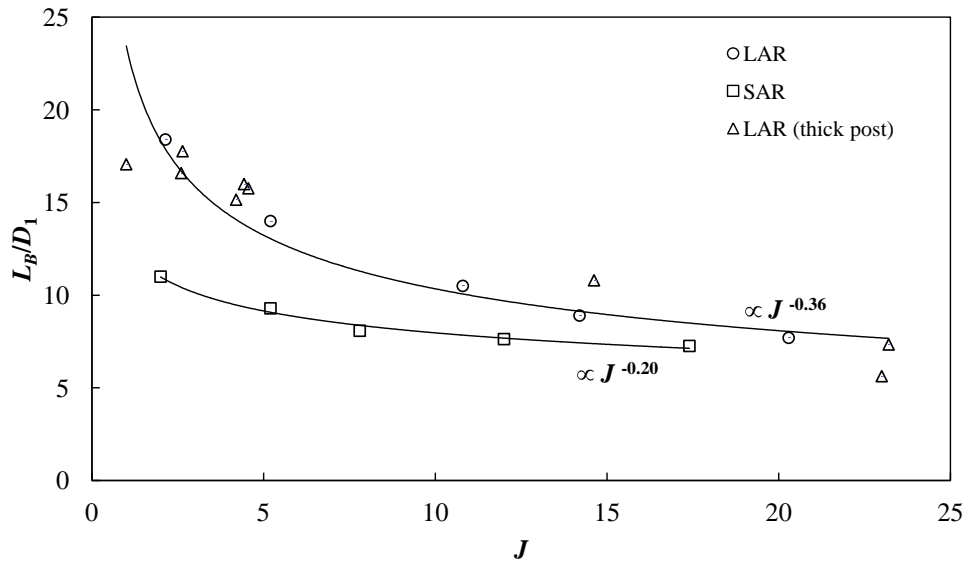


Figure 4. Back-lit images of baseline (a) LAR injector flows, and (b) SAR injector flows at $P_r = 0.44$.

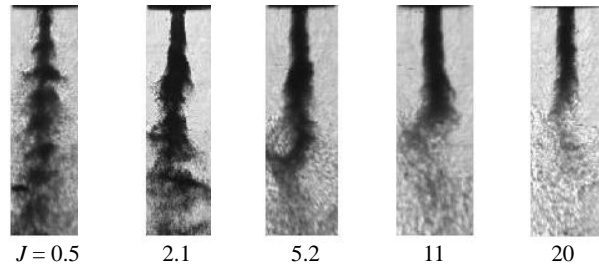


(a)

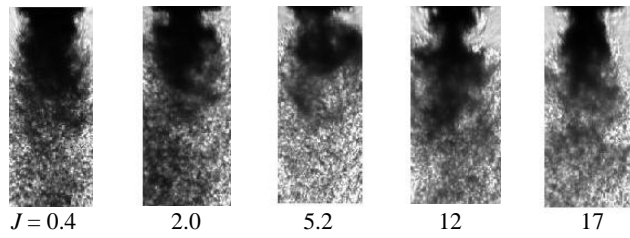


(b)

Figure 5. Normalized dark-core lengths (L_B/D_1) for baseline flow at $P_r = 0.44$: (a) LAR and SAR injector flows with uncertainties in individual L_B/D_1 measurements, and (b) power-fit for LAR, SAR, and LAR (with thick inner jet post¹⁷).



(a)



(b)

Figure 6. Back-lit images of PAN (a) LAR injector flows, and (b) SAR injector flows at $P_r = 0.44$.

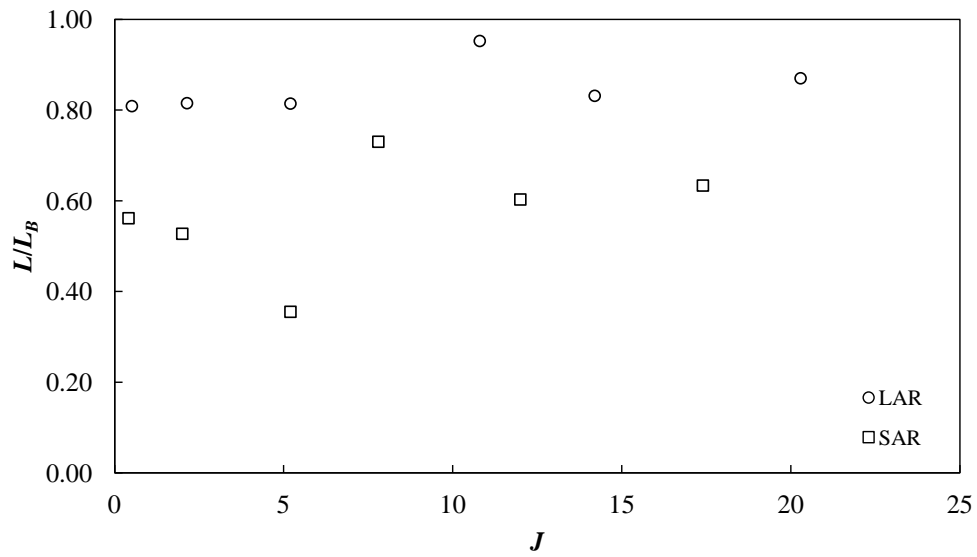


Figure 7. Dark-core lengths L normalized by baseline flow dark-core lengths L_B for PAN flow at $P_r = 0.44$.

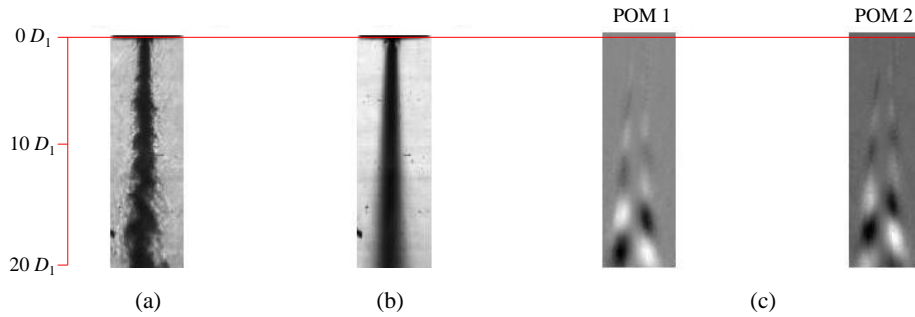


Figure 8. Baseline LAR injector flow at $P_r = 0.44$, $J = 0.5$: (a) snapshot image, (b) average image, (c) proper orthogonal mode (POM).

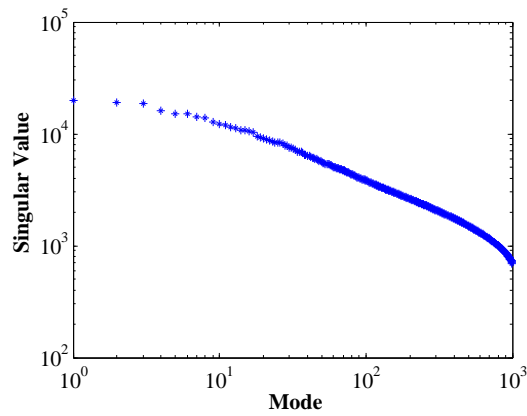


Figure 9. Singular values for baseline LAR injector flow at $P_r = 0.44$, $J = 0.5$.

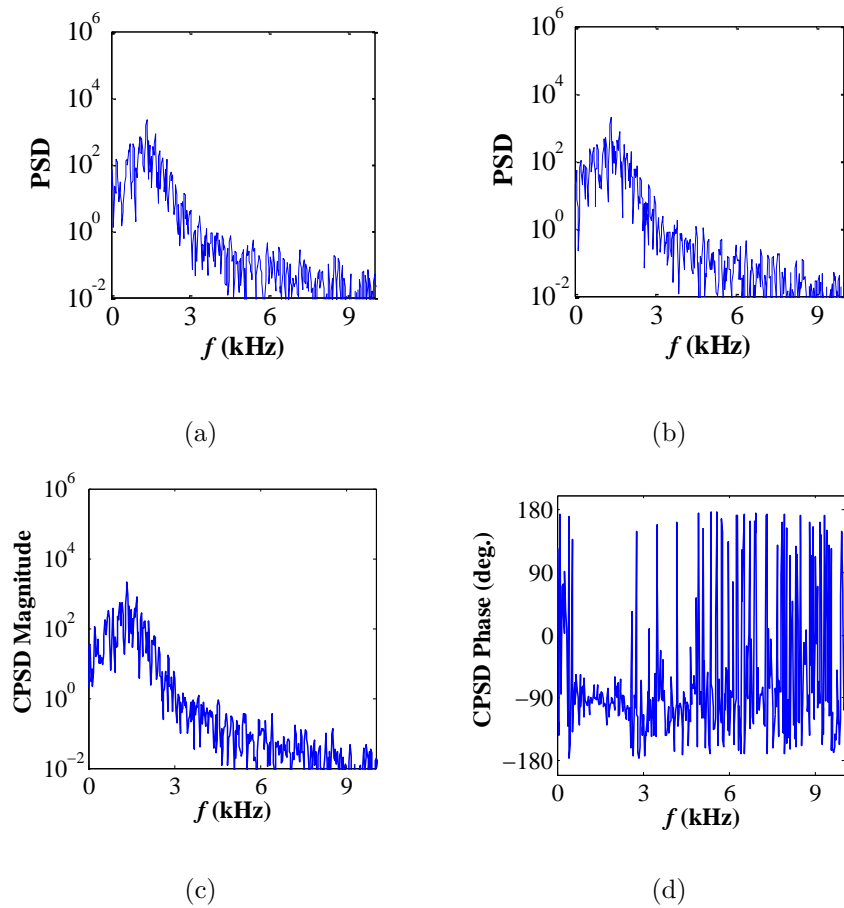


Figure 10. Baseline LAR injector flow at $P_r = 0.44$, $J = 0.5$: power spectral density (PSD) of the temporal amplitude coefficients of the decomposition corresponding to (a) POM 1, (b) POM 2, and cross-power spectral density (CPSD), (c) magnitude, (d) phase.

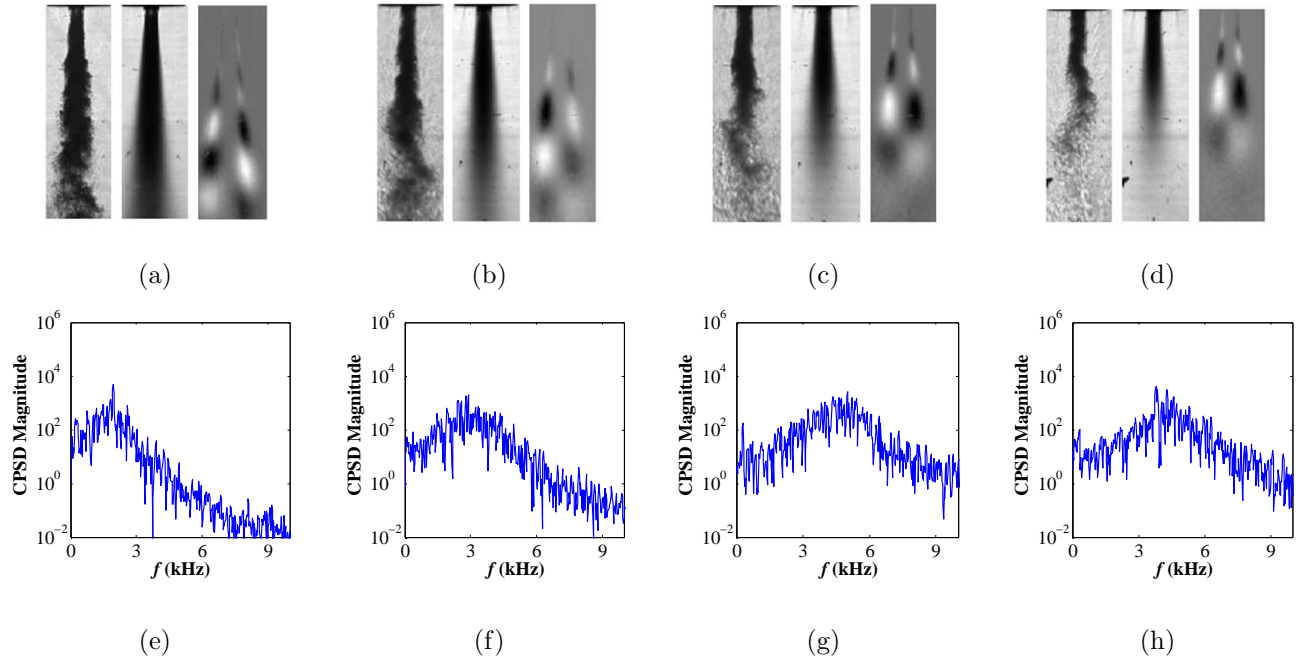


Figure 11. Baseline LAR injector flows at $P_r = 0.44$: snapshot, average, POM images for J (a) 2.1, (b) 5.2, (c) 11, (d) 20, and CPSD magnitude for J (e) 2.1, (f) 5.2, (g) 11, (h) 20.

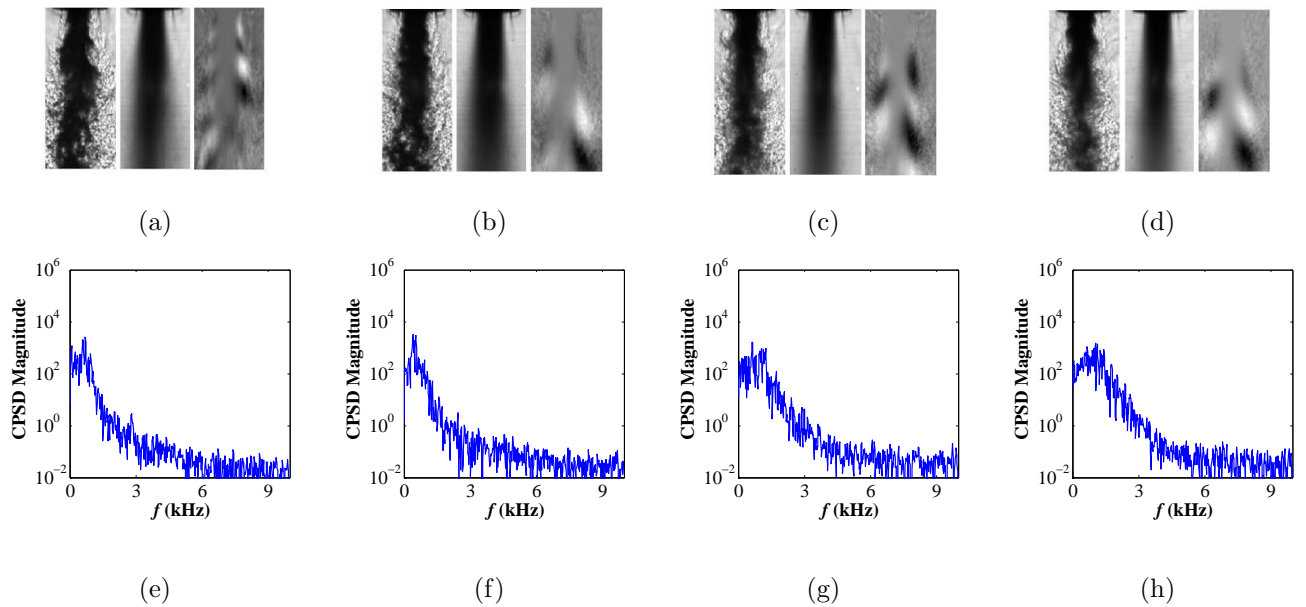
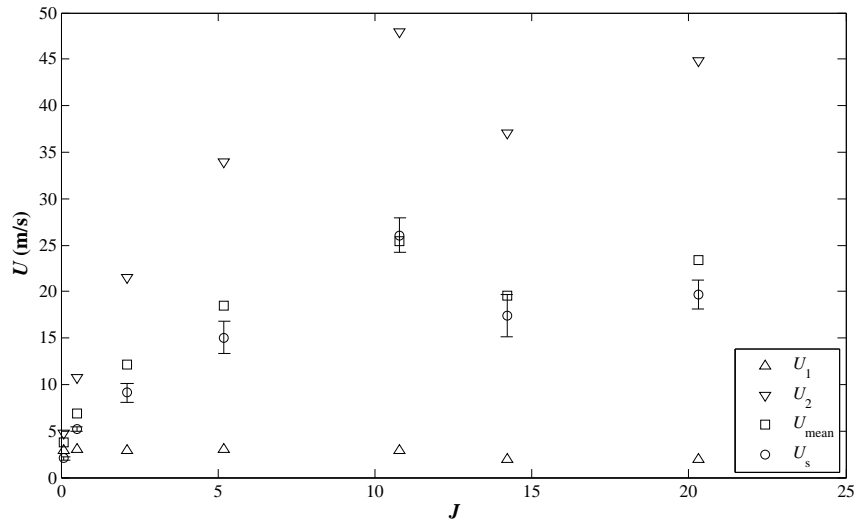
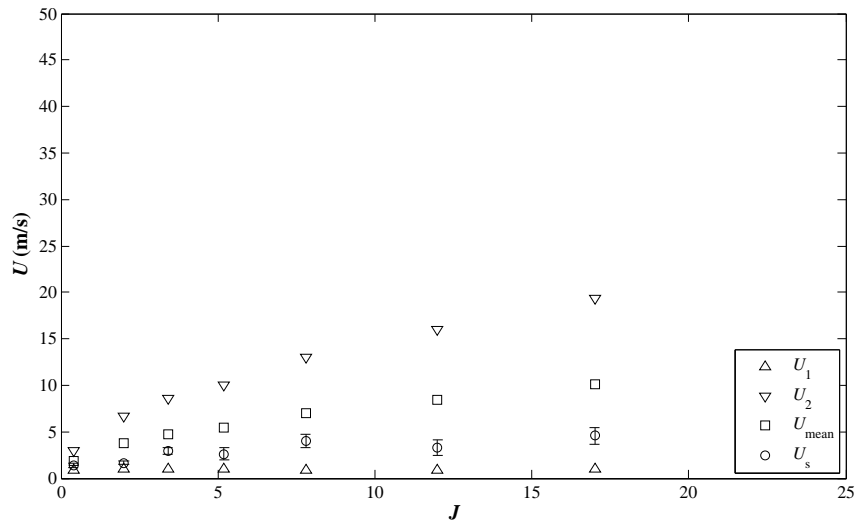


Figure 12. Baseline SAR injector flows at $P_r = 0.44$: snapshot, average, POM images for J (a) 0.5, (b) 1.9, (c) 5.0, (d) 12, and CPSD magnitude for J (e) 0.5, (f) 1.9, (g) 5.0, (h) 12.



(a)



(b)

Figure 13. Baseline velocities for (a) LAR injector flows, and (b) SAR injector flows at $P_r = 0.44$.

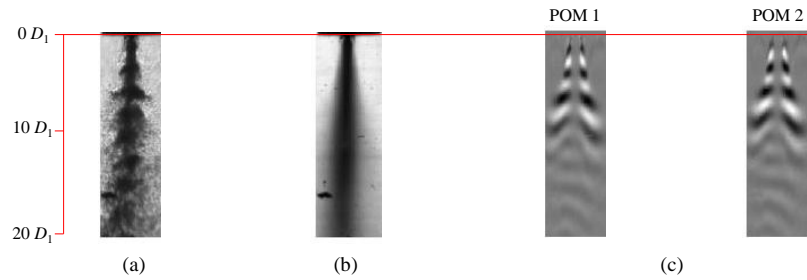


Figure 14. PAN forced ($f_F = 3.14$ kHz) LAR injector flow at $P_r = 0.44$, $J = 0.5$: (a) snapshot image, (b) average image, (c) proper orthogonal mode (POM).

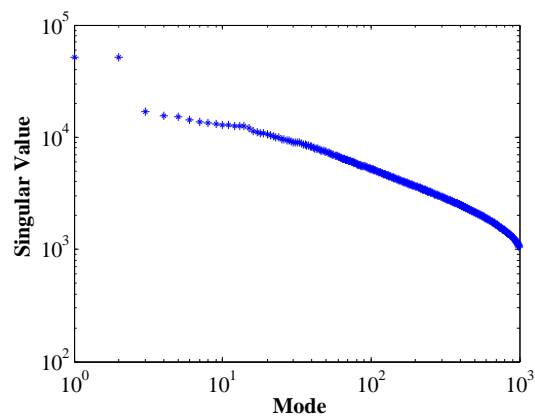


Figure 15. Singular values for PAN forced ($f_F = 3.14$ kHz) LAR injector flow at $P_r = 0.44$, $J = 0.5$.

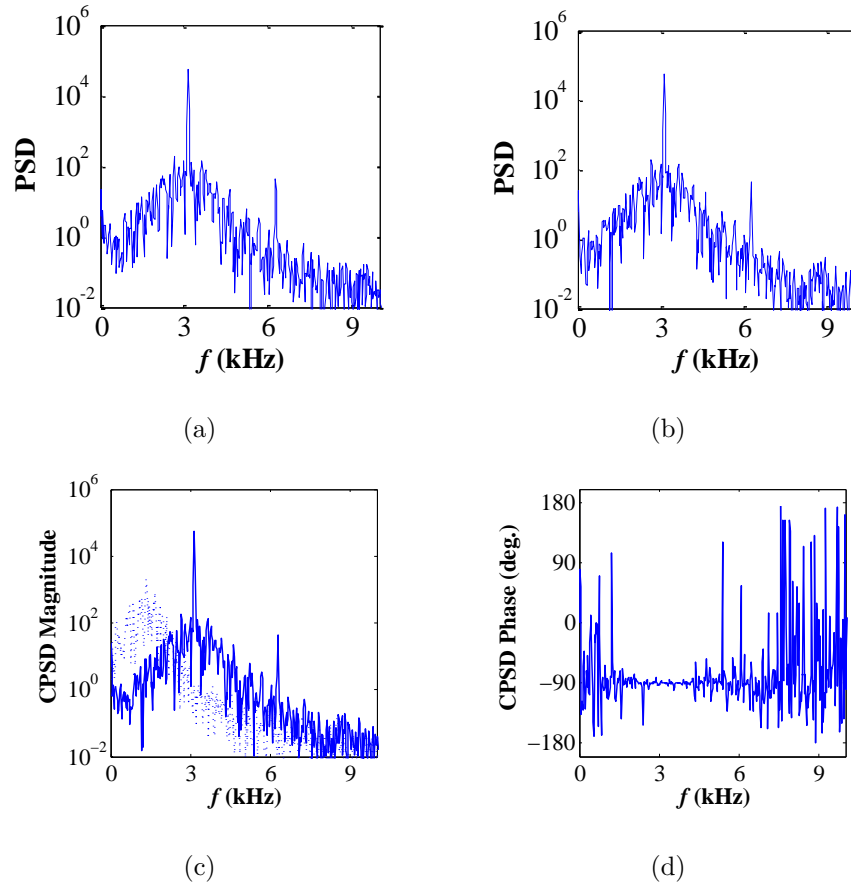


Figure 16. PAN forced ($f_F = 3.14$ kHz) LAR injector flow at $P_r = 0.44$, $J = 0.5$: power spectral density (PSD) of the temporal amplitude coefficients of the decomposition corresponding to (a) POM 1, (b) POM 2, and cross-power spectral density (CPSD) (c) magnitude, (d) phase. (.....Baseline, ——PAN)

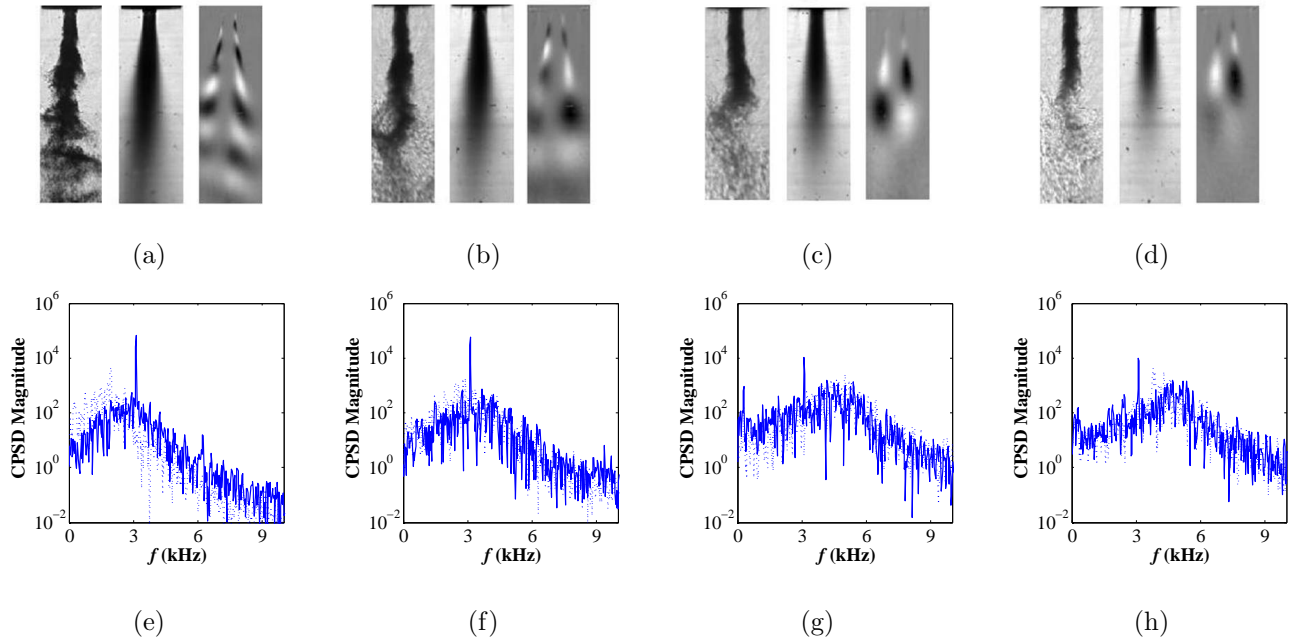


Figure 17. PAN forced LAR injector flows at $P_r = 0.44$: snapshot, average, POM images and CPSD magnitudes for J (a),(e) 2.1 ($f_F = 3.12$ kHz); (b),(f) 5.2 ($f_F = 3.12$ kHz); (c),(g) 11 ($f_F = 3.10$ kHz); (d),(h) 20 ($f_F = 3.11$ kHz). (.....Baseline, ——PAN)

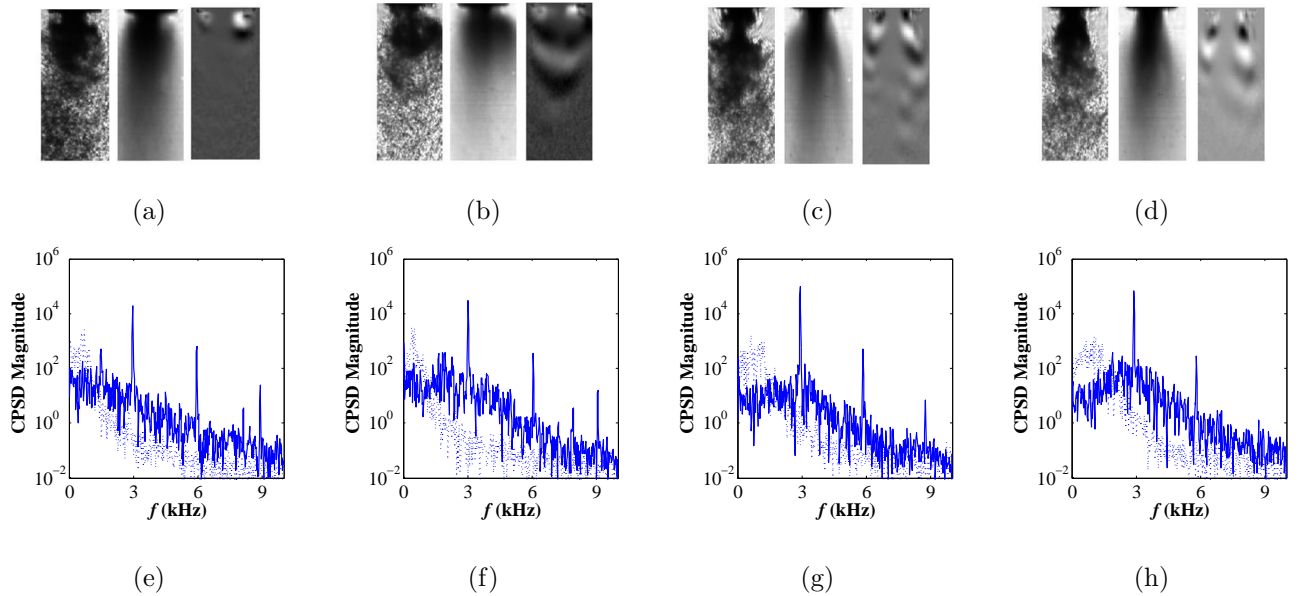


Figure 18. PAN forced SAR flows at $P_r = 0.44$: snapshot, average, POM images and CPSD magnitude for J (a) 0.5 ($f_F = 3.10$ kHz), (b) 1.9 ($f_F = 3.10$ kHz), (c) 5.0 ($f_F = 3.41$ kHz), (d) 12 ($f_F = 3.10$ kHz). (.....Baseline, ——PAN)

Appendix

Summary tables of flow conditions and parameters

LAR

J	R	T_{chamber} (K)	ρ_{chamber} (kg/m ³)	P_{chamber} (MPa)	T_o (K)	\dot{m}_o (mg/s)	ρ_o (kg/m ³)	U_o (m/s)	Re_o (10 ⁴)	T_i (K)	\dot{m}_i (mg/s)	ρ_i (kg/m ³)	U_i (m/s)	Re_i (10 ⁴)
0.5	3.5	217	24	1.50	204	1106	26	10.7	3.1	110	727	622	3.0	2.4
2.1	7.4	220	23	1.50	205	2212	25	21.5	6.3	107	725	646	2.9	2.1
5.2	11	221	23	1.50	203	3531	26	33.9	10	108	733	639	3.0	2.2
11	17	216	24	1.51	204	4991	26	47.9	14	107	722	646	2.9	2.1
20	22	220	23	1.50	204	4633	26	44.8	13	110	482	622	2.0	1.6

SAR

J	R	T_{chamber} (K)	ρ_{chamber} (kg/m ³)	P_{chamber} (MPa)	T_o (K)	\dot{m}_o (mg/s)	ρ_o (kg/m ³)	U_o (m/s)	Re_o (10 ⁴)	T_i (K)	\dot{m}_i (mg/s)	ρ_i (kg/m ³)	U_i (m/s)	Re_i (10 ⁴)
2.0	6.9	246	21	1.49	195	450	27	6.6	1.1	109	925	630	0.96	1.5
5.2	11	217	24	1.49	184	750	29	10	1.9	110	925	620	0.97	1.5
12	17	222	23	1.49	194	1100	27	16	2.6	108	925	640	0.94	1.4
17	20	217	24	1.48	194	1300	27	19.3	3.1	108	925	638	0.95	1.4